Available online at www.sciencedirect.com
SCIENCE DIRECT®
Acta Materialia 52 (2004) 5665–5675
Acta MATERIALIA
www.actamat-journals.com

Discrete dislocation density modelling of single phase FCC polycrystal aggregates

Ke-Shen Cheong [a,1], Esteban P. Busso [b,*]

[a] Materials Performance Technologies, Industrial Research Ltd., Lower Hutt 6009, New Zealand
[b] Department of Mechanical Engineering, Imperial College London, SW7-2AZ, UK

Received 11 May 2004; received in revised form 9 July 2004; accepted 23 August 2004
Available online 28 September 2004

Abstract

A new dislocation-mechanics based crystallographic theory has been developed to model the mechanical behaviour of single-phase FCC polycrystal aggregates. In the theory, dislocations are discretised into edge and screw components with intrinsically different relative mobilities and are subject to different dynamic recovery processes. The theory has been implemented within a finite-strain and rate-dependent constitutive framework, and applied to a thin polycrystal Cu specimen to investigate the effect of intragranular lattice misorientations on deformation behaviour. These misorientations are representative of low angle grain boundaries, which are known to play an important role in the microstructural evolution of polycrystals under monotonic and cyclic deformation. This study reveals that the presence of these misorientations strengthen the material response by suppressing and re-distributing the localisation of slip within the grains, as well as inhibiting the formation of sub-grains. Through the discretisation of dislocations, the model also predicts a higher proportion of edge dislocations in the vicinities of localised slip regions.

Keywords: Dislocations; Microstructure; Polycrystalline aggregates

1. Introduction

Texture development affects the formability and mechanical properties of many commercial alloys. A great deal of current research efforts focus on understanding and developing modelling tools to control the crystallographic textures so as to improve product performance [1–4]. At lower scales, the lattice misorientations at grain boundaries (intergranular) and within grains (intragranular) play a prominent role in the development of localised slip bands, leading to crack nucleation and ultimately, fracture. Intragranular misorientations usually develop as a result of anisotropic deformation, leading to the development of textures and dislocation cell structures. In polycrystalline aggregates, these cell structures are essentially low-angle boundaries which sub-divide each grain to produce inhomogeneities, and are generally observed in well-annealed metals [5]. The formation of cell structures, or 'polygonisation', often occur during the recovery stage of annealing processes [6]. On the basis of these observations, the common assumption that each grain in a polycrystalline aggregate can be uniquely described by a single lattice orientation is debatable. Strictly speaking, cell structures should also be accounted for since most polycrystalline metals, to some extent, undergo some form of heat-treatment prior to deformation and would inherently contain such inhomogeneities.

One of the main difficulties in carrying out detailed studies of deformation in polycrystalline aggregates lies in the complexity of the grain morphology. Each

* Corresponding author. Tel.: +44 207 594 7084; fax: +44 207 594 7017.
E-mail address: e.busso@imperial.ac.uk (E.P. Busso).
[1] Tel.: +64 493 130 92; fax: +64 493 134 31.

1359-6454/$30.00
doi:10.1016/j.actamat.2004.08.044

individual grain varies in shape and size, and there exists a multitude of grains through an aggregate of finite thickness that makes it difficult to accurately characterise its sub-surface structure using non-destructive techniques, such as orientation imaging microscopy (OIM). Thus, based on existing methods, a description of the constraints imposed by grains that are embedded beneath the surface constitutes a formidable challenge. To circumvent such limitations, quasi two-dimensional grain structures are used [7–10]. These 'multicrystals' essentially consists of a small quantity of large surface grains with a single grain layer through the thickness, and have gained popularity in recent years as they allow a direct comparison between numerical and experimental studies. By combining such grain structures with an appropriate crystallographic formulation based on microstructural internal state variables (e.g., dislocation densities), greater insight into the grain interaction and deformation behaviour of polycrystals can be achieved.

Typically, in dislocation density-based models, the evolution of the dislocation structure is described by processes of dislocation multiplication, annihilation as well as by the trapping of dislocations [3,11]. Further discretisation into pure edge and screw types enables their individual roles to be more clearly distinguished [12]. For example, edge and screw dislocations are associated with different dynamic recovery processes (i.e., climb for edges and cross-slip for screws), combining to influence the evolving dislocation structure of a deforming material. Moreover, it is now possible through X-ray profile analyses to quantify the edge and screw dislocation densities in deformed metals [13]. Therefore, the ability to make quantitative rather than just qualitative comparisons between predicted and measured dislocation densities constitute a powerful tool. However, the roles of edge and screw dislocations in determining the non-uniform distribution of plastic strain in polycrystals as a result of intergranular and intragranular interactions are still not well understood. Therefore, the aim of this study is to develop further insight into the interactions at the intergranular and intragranular levels, based on a fundamental understanding of the mechanics of dislocation motion and interaction.

In this work, a rate-dependent, dislocation mechanics-based crystallographic framework for finite strain is first presented to describe the constitutive behaviour of each single crystal grain. This includes the evolutionary laws for the dislocation densities discretised into edge and screw components. The single crystal model parameters are next identified for Cu by calibrating them against single crystal tensile test data. Finally, the model is applied to study the effects of misorientations in Cu multicrystals under uniaxial loading.

Throughout the paper, standard tensorial notation will be used. Vectors will be described by boldface lower case letters, second-order tensors by boldface upper case letters, and fourth-order tensors by italic upper case letters. Also, $\mathbf{ab} = a_i b_i, \mathbf{Ab} = A_{ij} b_j, \mathbf{A} : \mathbf{B} = A_{ij} B_{ij}, \mathbf{AB} = A_{ij} B_{jk}, \mathscr{C} : \mathbf{A} = C_{ijkl} A_{kl}, \mathbf{a} \otimes \mathbf{b} = a_i b_j$, where Einstein summation applies for repeated indices.

2. Constitutive framework

The foundations of the constitutive model for single crystal elasto-plastic finite-strain kinematics, uses the multiplicative decomposition of the total deformation gradient $\mathbf{F}$ [14]. For isothermal conditions,

$$\mathbf{F} = \mathbf{F}^{\mathrm{e}}\mathbf{F}^{\mathrm{p}}, \tag{1}$$

where $\mathbf{F}^{\mathrm{p}}$ is associated with crystallographic slip and $\mathbf{F}^{\mathrm{e}}$ describes the stretching and rotation of the crystal lattice. As the deformation history of the crystalline solid is important, it is essential to express $\mathbf{F}$ in rate-form,

$$\dot{\mathbf{F}} = \mathbf{L}\mathbf{F}, \tag{2}$$

where $\dot{\mathbf{F}}$ is the rate of the total deformation gradient and $\mathbf{L}$ is the spatial velocity gradient. Subsequently, $\mathbf{L}$ can be additively decomposed into its elastic ($\mathbf{L}^{\mathrm{e}}$) and plastic ($\mathbf{L}^{\mathrm{p}}$) counterparts,

$$\mathbf{L} = \dot{\mathbf{F}}^{\mathrm{e}}\mathbf{F}^{\mathrm{e}^{-1}} + \mathbf{F}^{\mathrm{e}}\dot{\mathbf{F}}^{\mathrm{p}}\mathbf{F}^{\mathrm{p}^{-1}}\mathbf{F}^{\mathrm{e}^{-1}} = \mathbf{L}^{\mathrm{e}} + \mathbf{F}^{\mathrm{e}}\mathbf{L}^{\mathrm{p}}\mathbf{F}^{\mathrm{e}^{-1}}. \tag{3}$$

From the kinematics of dislocation motion where plastic deformation is assumed to be solely the result of crystallographic slip, $\mathbf{L}^{\mathrm{p}}$ can be prescribed to be the sum of crystallographic slip rates on N number of activated slip systems [14],

$$\mathbf{L}^{\mathrm{p}} = \sum_{\alpha=1}^{N} \dot{\gamma}^{\alpha}\mathbf{P}^{\alpha}, \quad \mathbf{P}^{\alpha} \equiv \mathbf{m}^{\alpha} \otimes \mathbf{n}^{\alpha}. \tag{4}$$

Here, $\dot{\gamma}^{\alpha}$ is the crystallographic slip rate on a generic slip system α and $\mathbf{P}^{\alpha}$ is the generalised Schmid tensor formed from the dyadic product of the crystallographic slip direction and slip plane normal unit vectors in the reference configuration, $\mathbf{m}^{\alpha}$ and $\mathbf{n}^{\alpha}$, respectively. The time rate of change of the plastic deformation gradient, $\dot{\mathbf{F}}^{\mathrm{p}}$, is governed by,

$$\dot{\mathbf{F}}^{\mathrm{p}} = \mathbf{L}^{\mathrm{p}}\mathbf{F}^{\mathrm{p}}. \tag{5}$$

The elastic strain measure, $\mathbf{E}^{\mathrm{e}}$, work conjugate to the elastic Green–Lagrange strain tensor with respect to the intermediate configuration, is defined as,

$$\mathbf{E}^{\mathrm{e}} = \tfrac{1}{2}\left[\mathbf{F}^{\mathrm{e}\mathrm{T}}\mathbf{F}^{\mathrm{e}} - \mathbf{I}\right], \tag{6}$$

where $\mathbf{I}$ denotes the second-order identity tensor. Since the Cauchy stress tensor $\boldsymbol{\sigma}$ is not work-conjugate to any convenient measure of strain, the tensor $\mathbf{T}^{*}$, defined as the second Piola–Kirchhoff stress $\mathbf{T}$ pushed forward to the intermediate configuration, is introduced,

$$\mathbf{T}^{*} = (\det\ \mathbf{F}^{\mathrm{e}})\mathbf{F}^{\mathrm{e}^{-1}}\boldsymbol{\sigma}\mathbf{F}^{\mathrm{e}-\mathrm{T}}. \tag{7}$$

Since $\mathbf{T}^{*}$ is the work conjugate stress measure to the Green–Lagrange strain tensor $\mathbf{E}^{\mathrm{e}}$, a hyperelastic consti-

tutive law referred to the intermediate configuration is relied upon to describe the mechanical response of the single crystal. This allows the total stress-strain relationship to be obtained from the Helmholtz potential energy of the lattice per unit reference volume, U,

$$\mathbf{T}^* = \frac{\partial U}{\partial \mathbf{E}^e}. \tag{8}$$

Differentiating Eq. (8) with respect to $\mathbf{E}^e$ yields a fourth-order tensor $\mathscr{K}$,

$$\frac{\partial \mathbf{T}^*}{\partial \mathbf{E}^e} = \mathscr{K}, \quad \text{where } \mathscr{K} = \frac{\partial^2 U}{\partial \mathbf{E}^{e2}}. \tag{9}$$

In most crystalline metals, the elastic deformation range is infinitesimal when compared to the plastic strains. Therefore, $\mathscr{K}$ can be approximated by the fourth-order anisotropic elasticity tensor $\mathscr{C}$ and the final constitutive law given in Eq. (8) becomes,

$$\mathbf{T}^* \simeq \mathscr{C} : \mathbf{E}^e. \tag{10}$$

3. Flow rule

Since plastic flow due to dislocation motion is inherently rate-dependent even at low homologous temperatures [15], the proposed kinetic equation for the crystallographic slip rate $\dot{\gamma}^\alpha$ follows a function of the form [16],

$$\dot{\gamma}^\alpha = \dot{\gamma}_0 \exp\left[-\frac{F_0}{\kappa\theta}\left\{1 - \left\langle \frac{|\tau^\alpha| - S_T^\alpha}{\hat{\tau}} \right\rangle^p \right\}^q\right] \operatorname{sgn}(\tau^\alpha). \tag{11}$$

Here $F_0, \dot{\gamma}_0, p, q$ are the flow rule parameters while κ is the Boltzmann constant and θ is the absolute temperature. Also, F_0 is defined as the Helmholtz free energy of activation, which is the total energy needed to overcome short-range obstacles without the aid of an applied shear stress. The terms τ^α and S_T^α represent the resolved shear stress and total athermal slip resistance to dislocation motion, respectively. It should be noted that S_T^α is essentially athermal apart from a weak temperature dependence of the shear modulus μ. Furthermore, $\hat{\tau}$ can be obtained by extrapolating the lattice friction stress at 0 K, $\hat{\tau}_0$, with the shear moduli ratio at θ and 0 K [17],

$$\hat{\tau} = \hat{\tau}_0 \frac{\mu}{\mu_0}, \tag{12}$$

thus reducing all elastic interactions to 0 K.

4. Kinematics of dislocation motion

As edge and screw dislocations act as obstacles to dislocation motion in the form of forest dislocations, their densities (ρ_e^α for edge, ρ_s^α for screw) contribute to the total athermal slip resistance according to

$$S_T^\alpha = \lambda \mu b^\alpha \sqrt{\sum_{\beta=1}^{N} \left[h^{\alpha\beta}\left(\rho_e^\beta + \rho_s^\beta\right)\right]}. \tag{13}$$

Here, λ is a statistical coefficient which accounts for the deviation from regular spatial arrangements of the dislocations, b^α represents the magnitude of the Burgers vector, and $h^{\alpha\beta}$ is a dislocation interaction matrix defined as,

$$h^{\alpha\beta} = \omega_1 + (1 - \omega_2)\delta^{\alpha\beta}. \tag{14}$$

The terms ω_1 and ω_2 in Eq. (14) are the interaction coefficients and $\delta^{\alpha\beta}$ is the Kronecker Delta. To complete the set of constitutive relations, separate evolutionary equations are developed for both dislocation densities, with dislocation multiplication and annihilation forming the bases of their evolutionary behaviour.

4.1. Main dislocation generation mechanism

In single phase materials, the generation of dislocations is due mainly to the resistance to dislocation motion posed by forest dislocations acting as random obstacles. In this work, dislocation generation is assumed to be associated with the expansion of dislocation loops originating from existing Frank–Read type sources. Fig. 1 shows an idealised, expanding dislocation loop on an arbitrary active slip system α during a time interval dt. The loop is assumed to be rectangular, with straight edge and screw sides of lengths L_e^α and L_s^α, respectively. The change in dislocation densities ($\mathrm{d}\rho_i^\alpha$), where i refers to either edge (e) or screw (s) dislocations, is attributed to the increase in length of the individual dislocation segments ($\mathrm{d}L_i^\alpha$) expanding simultaneously within a control volume V,

$$\mathrm{d}\rho_i^\alpha = \frac{\mathrm{d}L_i^\alpha(t)}{V} \quad \text{for } i = \mathrm{e}, \mathrm{s}. \tag{15}$$

Considering an edge segment of the dislocation loop, its contribution to the plastic strain increment after a time interval dt is,

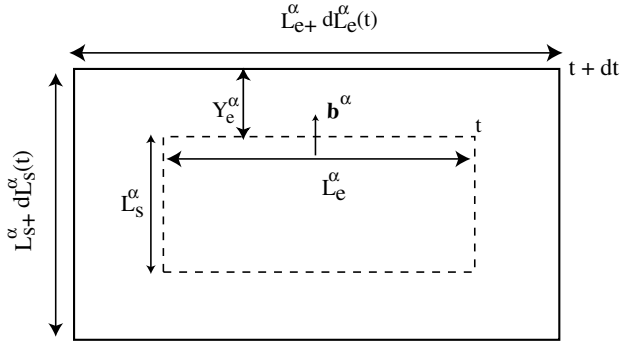

Fig. 1. Dislocation multiplication – schematic diagram of an idealised, expanding dislocation loop during a time interval dt.

$$\mathrm{d}\gamma_{\mathrm{e}}^{\alpha} = b^{\alpha} Y_{\mathrm{e}}^{\alpha} \left[\frac{L_{\mathrm{e}}^{\alpha} + \mathrm{d}L_{\mathrm{e}}^{\alpha}(t)}{V} \right]. \tag{16}$$

Here, Y_{e}^{α} is the mean free path of the edge dislocation segment, defined to be the distance travelled by the segment before its motion is arrested by forest dislocations (see Fig. 1). Differentiating Eq. (15) with respect to time yields the rate of generation of the edge dislocation density,

$$\dot{\rho}_{\mathrm{e,gen}}^{\alpha} = \frac{C_{\mathrm{e}}}{b^{\alpha} Y_{\mathrm{e}}^{\alpha}} \dot{\gamma}^{\alpha}, \tag{17}$$

and similarly for the generation of screw dislocations,

$$\dot{\rho}_{\mathrm{s,gen}}^{\alpha} = \frac{C_{\mathrm{s}}}{b^{\alpha} Y_{\mathrm{s}}^{\alpha}} \dot{\gamma}^{\alpha}. \tag{18}$$

In Eqs. (17) and (18), C_{e} and C_{s} are parameters which scale the magnitudes of the slip rate contributions from the edge and screw segments, respectively.

4.2. Main dislocation annihilation mechanism

In this work, mutual annihilation between parallel dislocations of the same character but opposite sign (herein defined as anti-parallel dislocations) is assumed to be the predominant annihilation mechanism. An annihilation event occurs when two dislocations are drawn towards each other by their attractive forces in order to reduce their line energies. Through this combination process, the opposing dislocations mutually annihilate. The probability of such an event occurring is determined by the cross-sectional area for annihilation. Such a region is illustrated by the dashed line in Fig. 2 around a gliding screw dislocation, which moves from the position at time "t" to "$t + \mathrm{d}t$". Here, the symbol d_{s} represents the critical distance for mutual annihilation between two anti-parallel screw dislocations to take place. Based on the region outlined in the figure, the annihilation area A_{s}^{α} for a screw segment gliding on an arbitrary slip system (α) is,

$$A_{\mathrm{s}}^{\alpha} = \left[2 d_{\mathrm{s}} Y_{\mathrm{s}}^{\alpha} + \pi d_{\mathrm{s}}^{2} \right]. \tag{19}$$

By combining Eqs. (15) and (19), the probability of an annihilation event is,

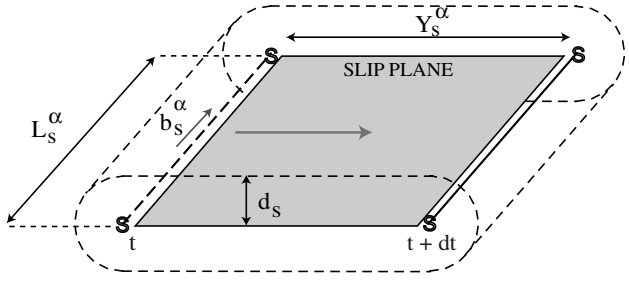

Fig. 2. Dislocation annihilation – schematic diagram of the annihilation region (dashed line) for a screw dislocation after a time interval dt.

$$P_{\mathrm{ann}} = \frac{1}{2} \left[\frac{A_{\mathrm{s}}^{\alpha} L_{\mathrm{s}}^{\alpha}}{V} \right] = \frac{A_{\mathrm{s}}^{\alpha} \rho_{\mathrm{s}}^{\alpha}}{2}, \tag{20}$$

where the factor of 1/2 in Eq. (20) assumes an equal density of anti-parallel screw dislocations. From the Orowan relationship [18], the rate of annihilation can be expressed as,

$$\dot{\rho}_{\mathrm{s,ann}}^{\alpha} = P_{\mathrm{ann}} \left[\frac{\dot{\gamma}_{\mathrm{s}}^{\alpha}}{b^{\alpha} Y_{\mathrm{s}}^{\alpha}} \right]. \tag{21}$$

It should be noted that the factor of 1/2 is eliminated since two screw dislocations are annihilated in every event. With Eqs. (19)–(21), the screw dislocation density annihilation rate is,

$$\dot{\rho}_{\mathrm{s,ann}}^{\alpha} = \frac{C_{\mathrm{s}}}{b^{\alpha}} \left[\frac{\pi d_{\mathrm{s}}^{2}}{Y_{\mathrm{s}}^{\alpha}} + 2 d_{\mathrm{s}} \right] \rho_{\mathrm{s}}^{\alpha} \dot{\gamma}^{\alpha}. \tag{22}$$

A similar expression obtained for edge dislocations does not include the additional term $\pi d_{\mathrm{s}}^{2} / Y_{\mathrm{s}}^{\alpha}$ due to its inability to cross-slip. Therefore, the edge dislocation annihilation rate is,

$$\dot{\rho}_{\mathrm{e,ann}}^{\alpha} = \frac{C_{\mathrm{e}}}{b^{\alpha}} \left[2 d_{\mathrm{e}} \rho_{\mathrm{e}}^{\alpha} \right] \dot{\gamma}^{\alpha}. \tag{23}$$

We note on passing that the critical edge annihilation distance d_{e} is smaller than the screw (i.e., $d_{\mathrm{e}} < d_{\mathrm{s}}$). To express the evolutionary laws for edge and screw dislocations in terms of their dislocation densities, Y_{e}^{α} and Y_{s}^{α} must be linked to the mean obstacle spacing, l_{m}^{α}, where the dominant obstacles are forest dislocations. A relationship between Y_{i}^{α} and l_{m}^{α} can be written as,

$$Y_{i}^{\alpha} = \frac{l_{m}^{\alpha}}{K_{i}} \quad \text{for } i = \mathrm{e}, \mathrm{s}, \tag{24}$$

where K_i is a dimensionless proportionality constant controlling the mobility of dislocations. Since a moving dislocation will be affected by the nature of the forest obstacle, i.e., edge and screw dislocations, the mean obstacle spacing l_{m}^{α} should be a function of the total dislocation density, $\rho_{\mathrm{T}}^{\alpha}$. Here, l_{m}^{α} follows the inverse-square root relationship obtained from geometric considerations,

$$l_{\mathrm{m}}^{\alpha} = \frac{1}{\sqrt{\sum_{\beta=1}^{N} \rho_{\mathrm{T}}^{\beta}}}. \tag{25}$$

The dislocation density evolutionary equations are formulated as balance equations (i.e., $\dot{\rho}_{i}^{\alpha} = \dot{\rho}_{i,\mathrm{gen}}^{\alpha} + \dot{\rho}_{i,\mathrm{ann}}^{\alpha}$). From Eqs. (17), (18) and (22)–(25), one obtains

$$\dot{\rho}_{\mathrm{e}}^{\alpha} = \frac{C_{\mathrm{e}}}{b^{\alpha}} \left[K_{\mathrm{e}} \sqrt{\sum_{\beta=1}^{N} \rho_{\mathrm{T}}^{\beta}} - 2 d_{\mathrm{e}} \rho_{\mathrm{e}}^{\alpha} \right] |\dot{\gamma}^{\alpha}|, \tag{26}$$

$$\dot{\rho}_{\mathrm{s}}^{\alpha} = \frac{C_{\mathrm{s}}}{b^{\alpha}} \left[K_{\mathrm{s}} \sqrt{\sum_{\beta=1}^{N} \rho_{\mathrm{T}}^{\beta}} - \rho_{\mathrm{s}}^{\alpha} \left(\pi d_{\mathrm{s}}^{2} K_{\mathrm{s}} \sqrt{\sum_{\beta=1}^{N} \rho_{T}^{\beta}} + 2 d_{\mathrm{s}} \right) \right] |\dot{\gamma}^{\alpha}|. \tag{27}$$

The constitutive model described above was numerically implemented into ABAQUS [19] as a user-defined material subroutine. Details of the numerical implementation into the finite-element (FE) method using an Euler backward (implicit) numerical integration scheme is given in a separate publication [20].

5. Calibration of the crystallographic formulation

5.1. Flow rule parameters

The flow rule defined by Eq. (11) contains five parameters $(\dot{\gamma}_0, F_0, \hat{\tau}_0, p, q)$ to be determined, two of which, namely F_0 and $\hat{\tau}_0$, are derived from experimental data. To determine F_0, it is useful to re-write Eq. (11) to express the flow stress dependence on temperature, strain rate and microstructural state,

$$\tau^{\alpha} = \hat{\tau}_0 \frac{\mu}{\mu_0}\left[1 - \left(\frac{\theta}{\theta_C}\right)^{1/q}\right]^{1/p} + S_0^{\alpha}\frac{\mu}{\mu_0}, \tag{28}$$

where

$$\theta_C = \left[\frac{F_0}{k\,\ln(\dot{\gamma}_0/|\dot{\gamma}^{\alpha}|)}\right] \tag{29}$$

is a critical temperature above which, all short-range obstacles can be overcome by thermal activation. An estimate for F_0 was found using the saturation stress of [0 0 1]-oriented Cu single crystal in tension at 1073 K under an applied strain rate of 3.0×10^{-3} s^{-1} [21]. The corresponding slip rate is calculated to be $\dot{\gamma}^{\alpha} = \dot{\epsilon}_{0\,0\,1}/(1/\sqrt{6}) = 7.35\times10^{-3}$ s^{-1}, where $1/\sqrt{6}$ is the Schmid factor of the [0 0 1] loaded crystal. From Eq. (29), using $\theta_C = 1073$ K, an approximation of F_0 is 2.77×10^{-19} J.

The mechanical threshold $\hat{\tau}_0$ is determined from the temperature sensitivity of the yield stress of Cu polycrystals [22], scaled with the temperature-dependent elastic modulus ratio E_0/E_T (see Fig. 3). The yield stress at absolute zero ($\sigma_{Y,0\ K}$) is estimated by extrapolating the data to 0 K, while the athermal component of the yield strength, $\sigma_{Y,sat}$, is obtained when σ_Y approaches its asymptotic value at high temperatures. By taking the Taylor factor for FCC polycrystalline metals with random texture (i.e., $M = 3.06$) to obtain the critical shear stress, a generic expression for $\hat{\tau}_0$ can be obtained,

$$\hat{\tau}_0 = \left[\frac{\sigma_{Y,0\ K} - \sigma_{Y,sat}}{M}\right]. \tag{30}$$

For Cu, $\hat{\tau}_0$ was determined to be 20.0 MPa.

The remaining flow rule parameters, namely $\dot{\gamma}_0, p$ and q, were chosen to lie between ranges suggested by Kocks [23],

$$10^6 \leqslant \dot{\gamma}_0 \leqslant 10^7\ \text{s}^{-1}, \tag{31}$$

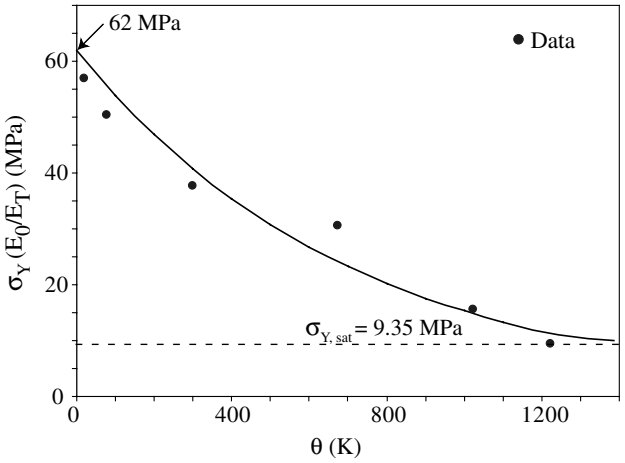

Fig. 3. Temperature variation of the yield stress σ_Y for Cu scaled by the ratio (E_0/E_T). (Data from [22].)

$$0 \leqslant p \leqslant 1, \tag{32}$$

$$1 \leqslant q \leqslant 2. \tag{33}$$

For Cu, these parameters were chosen to lie within the specified ranges, close to those of Al [24]. The final values are given in Table 1.

5.2. Material constants, loading and boundary conditions

The initial value for the total dislocation density, ρ_T^{α}, was assumed to be typical of most annealed pure FCC single crystals and equal to 16,000 mm^{-2}. Furthermore, the initial dislocation population was considered to be made up of an equal proportion of edge and screw components. The statistical coefficient λ in Eq. (13) was assigned a value of 0.3 based on the work by Kuhlmann–Wilsdorf [26] and Basinski et al. [27]. To account for latent hardening effects, the ω_1 and ω_2 components of the dislocation interaction matrix $h^{\alpha\beta}$ (Eq. (14)) were chosen to be 1.5 and 1.2, respectively. This compares closely to the average latent hardening ratios of Cu [28].

To keep the same slip contributions from both dislocation types, the parameters C_e and C_s in Eqs. (17) and (18) were set to 0.5. Furthermore, previous slip line measurements on Cu and Al [29–31] consistently reported the distance travelled by edge dislocations to be approximately twice that of screw dislocations. Since this is intrinsically linked to the mean free paths of the two dislocation types, the parameter K_s in Eq. (24) is specified to be twice that of K_e (i.e., $K_s = 2K_e$). By further relying on the theoretical estimate of d_e to be of

Table 1
Flow rule parameters (Eq. (11) for Cu)

$\hat{\tau}_0$ (MPa)	p	q	$\dot{\gamma}_0$ (s^{-1})	F_0 (J)
20.0	0.2	1.2	1.00×10^6	2.77×10^{-19}

the order of 1.0 nm [32], the number of parameters to be determined is now reduced to two (i.e., K_s, d_s).

In determining the set of hardening-recovery parameters from Eqs. (26) and (27) (namely d_e, d_s, K_e, K_s), the constitutive model response was calibrated against high-symmetry tensile test data of Cu single crystals at 295 K. To simulate the uniaxial tensile tests, a 3D FE model of a rectangular bar consisting of $45 \times 5 \times 2$ quadratic brick elements with reduced integration was used. Appropriate boundary conditions were specified such that both the front and back faces of the mesh remained parallel to each other and normal to the loading direction throughout the analysis. A displacement-controlled load was applied at one end of the specimen at a true strain rate of 3.0×10^{-3} s^{-1}. In all cases, fixed misalignments of 0.5° from the [1 0 0], [1 1 1] and [1 1 2] crystal orientations were introduced to account for the initial misorientations reported in the data. To fit the data, d_s and K_s/b^α were set to 5 nm and 110×10^3 mm^{-1}, respectively (see also Table 2). From Eq. (24), this corresponds to initial mean free paths of $Y_e^\alpha = 80.7$ and $Y_s^\alpha = 161.4$ μm for edge and screw dislocations, respectively. These values are in good agreement with the estimated initial slip distances of edge (~ 100 μm) and screw (~ 200) dislocations on [1 1 2]-oriented Cu single crystals [33]. Fig. 4(a) shows the comparisons between the model predictions and the experimental data, with 5% error bars added to show the goodness of fit. As indicated in the figure, there is good agreement for the [1 1 1] orientation but less so for the other two orientations. However, in modelling polycrystal behaviour, it is more essential that the model accurately predicts the different work-hardening rates. Fig. 4(b) shows the associated work-hardening rates ($d\sigma/d\varepsilon$), in logarithmic scale, in terms of the applied true strain along the different crystallographic orientations. It can be seen that the experimental and predicted trends are in good agreement for all three crystal orientations. It should be noted that the fluctuations in the experimental work-hardening rates is a consequence of the numerical differentiation of the stress–strain data and therefore, no error bars are shown in Fig. 4(b).

Table 2
Model parameters for Cu

From Eqs. (13), (24), (26) and (27)	C_i	K_i/b^α (mm^{-1})	d_i (nm)	Y_i^α (μm)
Edge (i = e)	0.5	55×10^3	1.0	80.7
Screw (i = s)	0.5	110×10^3	5.0	161.4
μ = 45.0 GPa	λ = 0.3	b^α = 0.257 nm	ω_1 = 1.5	ω_2 = 1.2

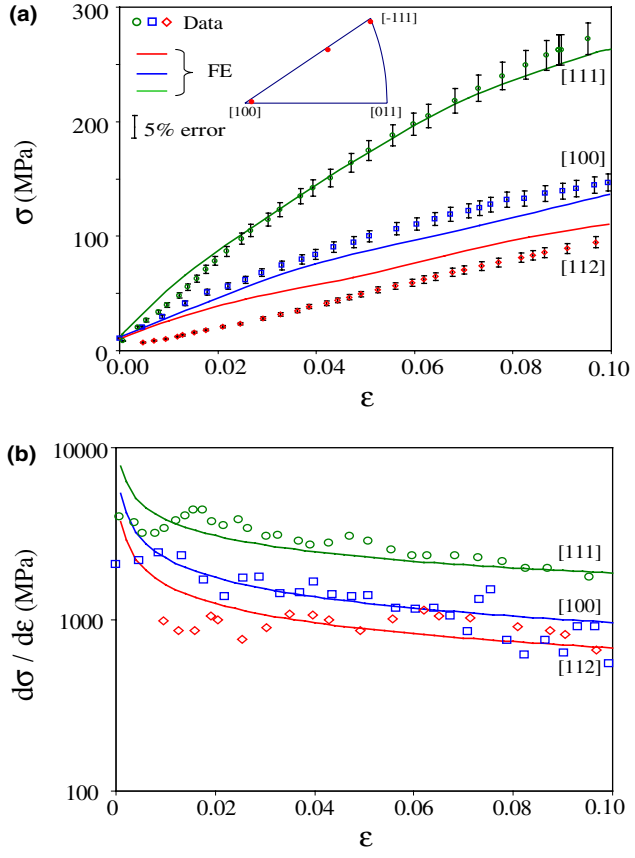

Fig. 4. (a) True-stress–strain predictions with experimental data [25] and (b) work-hardening rate ($d\sigma/d\varepsilon$) against true strain, for Cu crystals at θ = 295 K as a function of orientation.

6. Application of the crystallographic model to Cu aggregates

As previously discussed, in deformation studies of polycrystalline aggregates, it is commonplace to treat the lattice orientation within each grain to be uniform. However, experimental evidence indicates that substructure networks exist even in grains of well-annealed metals [34,35]. Unlike high-angle grain boundaries, these substructures are essentially low-angle boundaries where the orientation across a boundary is only several degrees apart. These misorientations arise from the rearrangement of dislocation arrays and they encompass a range of microstructural features such as dislocation cells, veins, annealing twins etc. Therefore, a more complete description of the microstructure will require the consideration of lattice misorientations associated with these substructure features. Microstructure characterisation tools, such as electron back scattering diffraction (EBSD) techniques, can be used to accurately construct microstructures containing these small misorientations. Fig. 5 shows an EBSD orientation map of the longitudinal section of a directionally-solidified Ni-based alloy and the misorientation profile along one of the grains. The profile indicates that the orientation along the direction of solidification is not uniform but contains a misorientation distribution of up to 5°. Further evidence of intragranular misorientations has also been reported in polycrystalline Ag [35].

In this section, the influence of grain substructures on material behaviour is studied using a Cu multicrystal consisting of 11 mm-sized grains. The use of multicrystals is particularly appropriate for such a study as intergranular interactions are kept to a minimum. First, comparisons are made between the mechanical response of an 'idealised' multicrystal, where the grain orientations are assumed to be uniform and cases where the local orientation within each grain has been perturbed to introduce intragranular misorientations. Three cases were considered: Case A assumes the lattice orientation within each grain to be uniform. In Cases B and C, the initial orientation at each material point was perturbed to produce random misorientations ξ, ranging between 0° and 3° and 0° to 6°, respectively. The defined range of misorientation angles within each grain was based on the understanding that intragranular misorientations of up to 6° are typical in polycrystalline aggregates [37]. Fig. 6 shows the initial lattice orientation microstructural maps and their distributions on inverse-pole figures. Finally, the FE model of the polycrystal specimen, which is made up of 1834 quadratic brick elements with reduced integration, is shown in Fig. 7.

6.1. Effects of intragranular misorientations

To simulate the tensile tests, appropriate boundary conditions were applied to replicate the gripping action at each end of the specimen. A constant displacement rate, normalised by its initial length L_0 ($= 4 \times 10^{-4}$ s^{-1}) was imposed along the X_1 direction at one end while holding the other end rigidly (see Fig. 7). Fig. 8 shows the predicted force–displacement responses from the three case studies together with the experimental data at 295 K, with 5% error bars again added to the experimental data to show the goodness of fit with the FE simulations. When treating orientations within grains to be uniform (i.e., Case A), the predicted response agrees well with the data up to a displacement of 3 mm, beyond which it begins to deviate. For Cases B and C, it is observed that, at small displacements, the intragranular misorientation effect is negligible but becomes increasingly prominent beyond an extension of 3 mm. By introducing larger misorientations, the predicted macroscopic response increases. For Case C, good agreement (within 5% error) between the prediction and data is obtained even at larger extensions. At an extension of 3.7 mm, the lattice rotations predicted in grains $G1$, $G4$ and $G6$ for Cases A and C are plotted on inverse pole figures and compared with the experimental data in Fig. 9. As the extension is small, both cases show good agreement with the data with the exception of grain $G6$ in Case C, where a much larger scatter is observed. This is a result of the introduction of the intragranular misorientations, whereas the rotations predicted in Case A are sharper. In Fig. 10, contour plots of accumulated slip (ε^{p}) after an extension of 15 mm at the end of the analyses are shown for Cases A and C. For the Case A simulation, a highly localised region of extensive slip occurs across grains $G3$, $G4$ and $G9$ of the multicrystal. Similar to the FE results presented by Delaire [9], the highly localised accumulated slip across these grains is approximately three times the macroscopic strain. Crucially, these three grains span the entire cross-sectional width of the specimen, indicating that the strong build-up of accumulated slip led to the observed softening effect and lower overall response. However, such severe strain localisation is not observed in Case C. Here, the presence of the intragranular misorientations lessens the concentration of accumulated slip in localised regions in any one grain. Instead, the plastic strain is more uniformly redistributed to the neighbouring grains. In effect, this results in a higher work hardening rate than that observed in Case A, leading to a stronger macroscopic response.

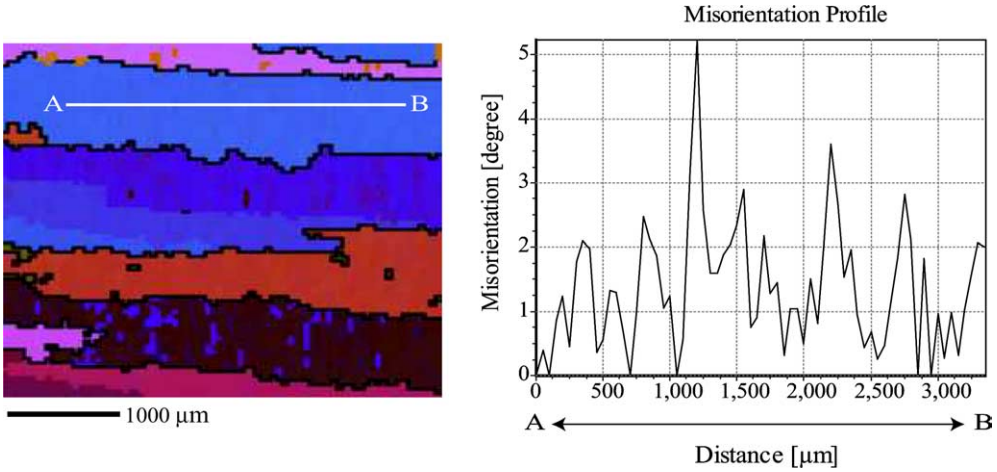

Fig. 5. EBSD orientation map of a directionally solidified Ni-based alloy and intragranular misorientation profile from A to B. Bold lines on EBSD map represent high angle grain boundaries with misorientations greater than 10°.

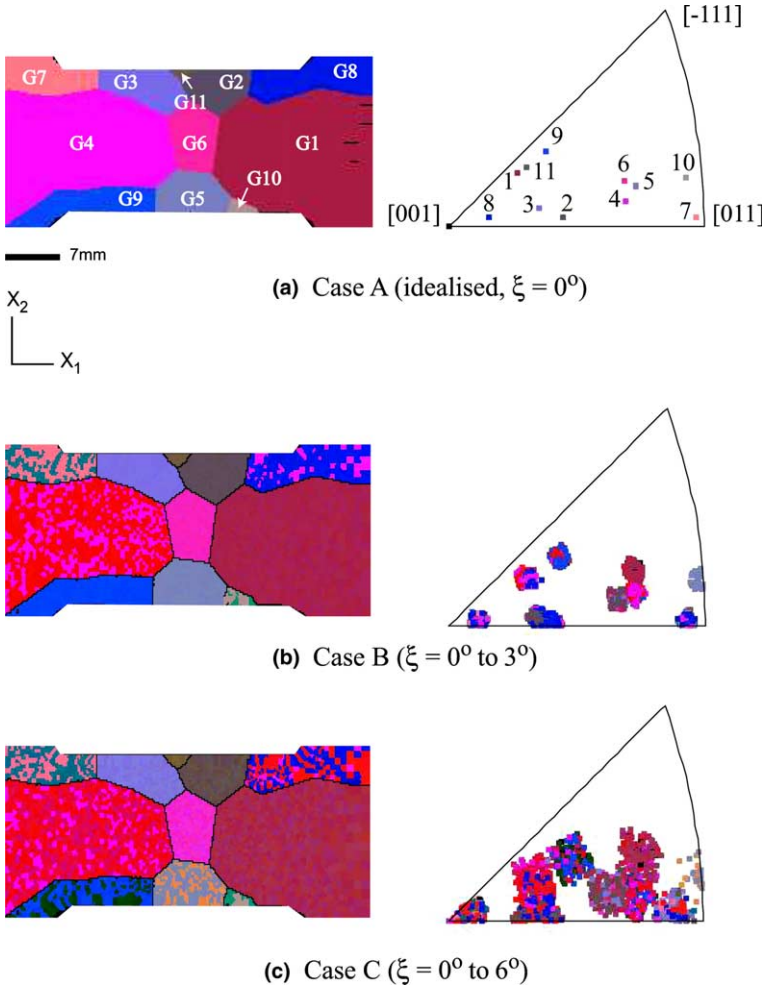

Fig. 6. Initial orientation of the multicrystal specimen plotted on microstructural maps and inverse-pole figures for the three case studies: (a) Case A – 'idealised' grains with uniform orientations, $\xi = 0°$, (b) Case B – misorientations ranging from $\xi = 0°$ to 3°, and (c) Case C – misorientations ranging from $\xi = 0°$ to 6°.

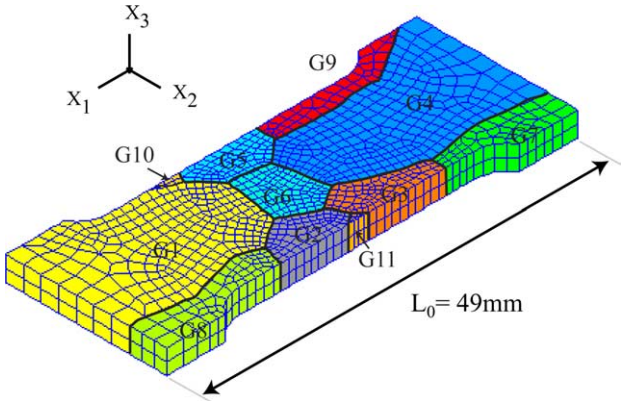

Fig. 7. FE model of the Cu multicrystal used to carry out intragranular misorientation studies.

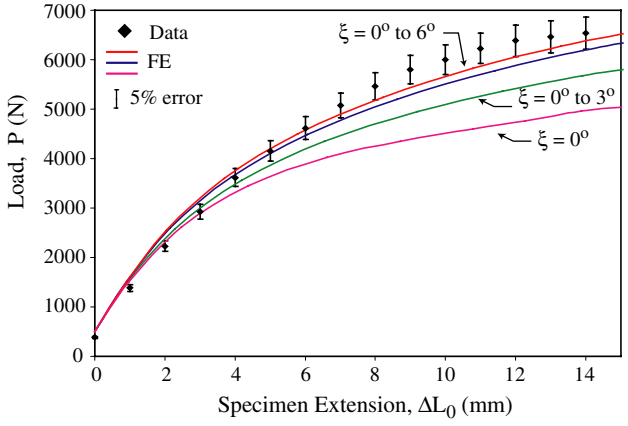

Fig. 8. Comparison between force-extension predictions for Cases A, B, C and the experimental data from Delaire [36].

In Fig. 11, the striking difference in lattice rotation between the two multicrystals at $\Delta L_0 = 15$ mm, is highlighted by the colour contrast from these microstructural maps. This observation is most apparent in *G*6, where the grain is entirely surrounded by neighbouring grains. In Case A, the local lattice rotation within *G*6

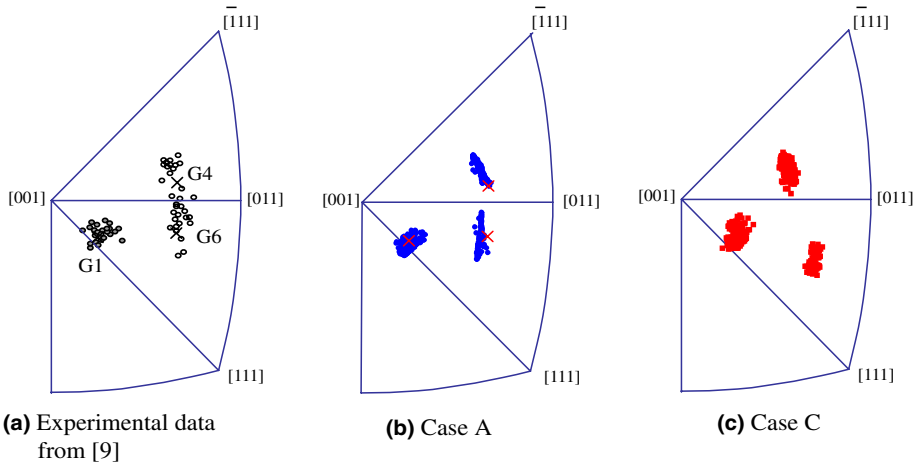

Fig. 9. Comparison between inverse pole figures for grains $G1$, $G4$ and $G6$: (a) Experimental data from [9], (b) Case A ($\xi = 0°$) and (c) Case C ($\xi = 0°$ to 6°), where 'X' indicates the initial orientations.

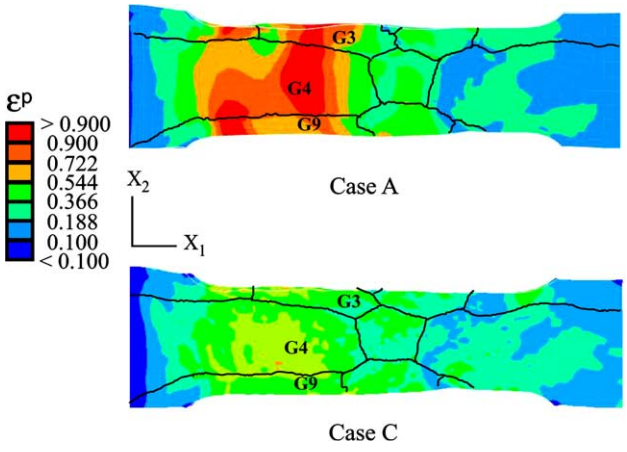

Fig. 10. Contour plots of accumulated slip (ε^p) at $\Delta L_0 = 15$ mm for Cases A and C.

leads to a subdivision into two separate regions of different orientations. As illustrated by the corresponding inverse pole figure, a fraction of the grain rotates towards the stable [0 0 1]–[$\bar{1}$ 1 1] symmetry boundary line, while the other rotates towards the [0 0 1]–[0 1 1] boundary. In contrast for Case C, the inverse pole figure shows that, the grain as a whole, is rotating towards the [0 0 1]–[$\bar{1}$ 1 1] symmetry boundary, as a result of introducing misorientations within the grain. Invariably, this implies that the presence of intragranular misorientations suppresses sub-grain formation in $G6$. Since the model discretises dislocation densities into edge and screw types, it is worth observing their distributions within the deformed multicrystals. Instead of plotting the distribution of each quantity separately, the edge and screw dislocation densities on the twelve potentially

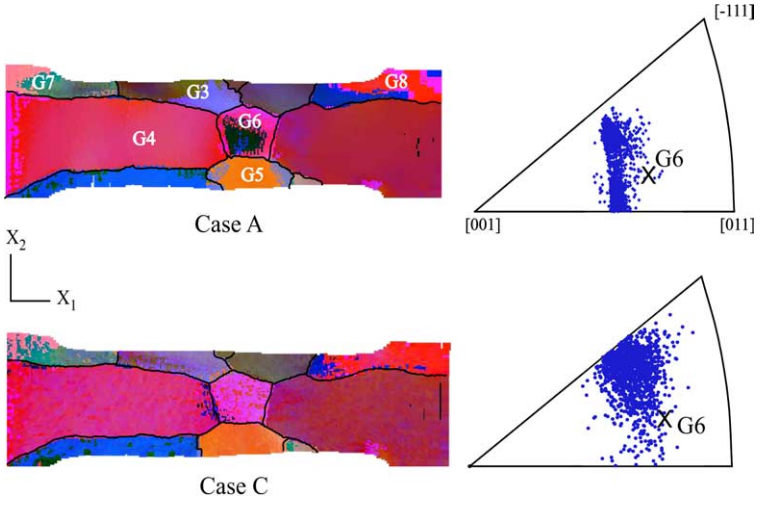

Fig. 11. Microstructural maps of lattice orientations at $\Delta L_0 = 15$ mm for Cases A and C with respective inverse-pole figures of grain $G6$ after deformation. ('X' marks the approximate region of the initial average grain orientation of $G6$.)

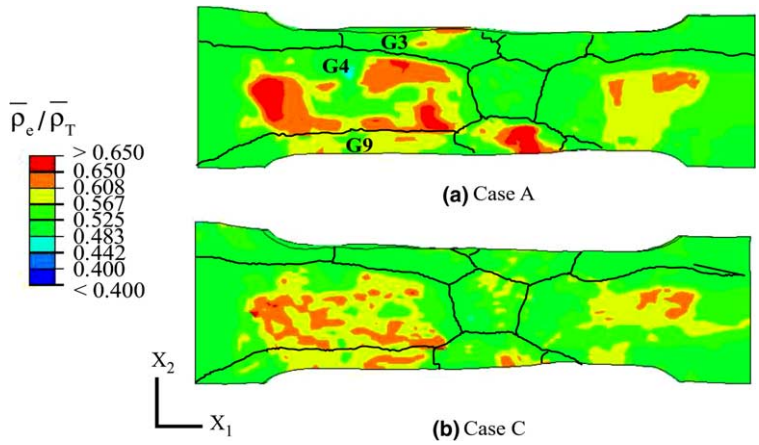

Fig. 12. Distribution of the average edge to total dislocation density ratio $\bar{\rho}_e/\bar{\rho}_T$ for (a) Case A and (b) Case C, at $\Delta L_0 = 15$ mm.

active $\{1\,1\,1\}\langle 1\,1\,0\rangle$ slip systems are averaged and shown in terms of $\bar{\rho}_e/\bar{\rho}_T$ in Fig. 12 for the cases (a) A and (b) C. It is interesting to note that in both cases, the model predicts a fairly homogeneous distribution of $\bar{\rho}_e/\bar{\rho}_T$ in several grains, together with a higher proportion of edge to screw dislocations in the band of localised accumulated slip (i.e., grains *G*3, *G*4 and *G*9). This effect is less apparent in Case C, consistent with a lower maxima in the band of localised slip. It was established that in these grains, only single and/or double slip were active whereas more than two slip systems were activated in the other grains. With more active slip systems, a lower $\bar{\rho}_e/\bar{\rho}_T$ ratio ensues as a result of the lower mobility of screw dislocations leading to a higher multiplication rate of screw to edge dislocations.

7. Conclusions

It has been shown that intragranular misorientations introduced by perturbing the average grain orientation is a simple, yet effective way of incorporating the effects of a non-uniform dislocation network (e.g., heterogeneities associated with low-angle grain boundaries). When grains are treated as discrete entities, the development of these substructures are not correctly accounted for, and a more rapidly developing texture is predicted. From a simple multicrystal study, it has been shown that intragranular misorientation effects are negligible when strains are small, but become increasingly significant at larger strains. The prediction of the experimentally measured macroscopic response of the multicrystal and grain orientations was achieved indirectly by introducing low-angle grain boundaries through intragranular misorientations. These low-angle boundaries suppressed and redistributed the concentration of slip, thus avoiding the formation of slip bands, which was evident when such misorientations were not accounted for. Moreover, these misorientations were also found to inhibit simultaneously the formation of sub-grains. Through the discretisation of dislocation densities, the model also revealed a greater density of edge dislocations in the regions of localised slip.

Acknowledgements

Financial support from ALSTOM Power, the Department of Trade and Industry and the Engineering and Physical Research Council of the United Kingdom through Grant GR/N12312, and the provisions of the specifications and experimental data for the Cu multicrystal by Drs. F. Delaire, J. L. Raphanel and C. Rey (Ecole Centrale de Paris, France) are gratefully acknowledged.

References

[1] Bronkhorst CA, Kalidindi SR, Anand L. Polycrystalline plasticity and the evolution of crystallographic texture in fcc metals. Philos Trans: Phys Sci Eng V 1992;341(1662):443–77.
[2] Becker R, Panchanadeeswaran S. Effects of grain interactions on deformation and local texture in polycrystals. Acta Mater 1995;43(7):2701–19.
[3] Peeters B, Seefeldt M, Teodosiu C, Kalidindi SR, VanHoutte P, Aernoudt E. Work-hardening/softening behaviour of B.C.C. polycrystals udring changing strain paths: I. An integrated model based on substructure and texture evolution, and its prediction of the stress–strain behaviour of an IF steel during two-stage strain paths. Acta Mater V 2001;49:1607–19.
[4] Raabe D, Roters F. Using texture components in crystal plasticity finite element simulations. Int J Plasticity 2004;20:339–61.
[5] Hansen N, Huang X. Microstructure and flow stress of polycrystals and single crystals. Acta Mater 1997;46(5):1827–36.
[6] Chu D, Morris Jr JW. The influence of microstructure on work hardening in aluminium. Acta Mater V 1996;44(7):2599–610.
[7] Teodosiu C, Raphanel JL, Tabourot L, Finite element simulation of the large elastoplastic deformation of multicrystals. In: Teodosiu C, Raphanel JL, Tabourout L, Sidoroff F, editors. Proceedings of the international seminar MECAMAT'91: Large

plastic deformations, fundamental aspects and applications to metal forming, Fontainebleau, France; 1991. p. 153–68.
[8] Becker R. Modeling of a clumnar grain polycrystal deformed in plane strain compression. In: Bieler TR, Lalli LA, MacEwen SR, editors. Proceedings of the 2nd TMS symposium: hot deformation of aluminum alloys II; 1998. p. 255–66.
[9] Delaire F, Raphanel JL, Rey C. Plastic heterogeneities of a copper multicrystal deformed in uniaxial tension: experimental study and finite element simulations. Acta Mater 2000;48:1075–87.
[10] Busso EP, Cheong KS. Length scale effects on the macroscopic behaviour of single and polycrystalline FCC crystals. J Phys IV 2001;11(Pr 5):161–9.
[11] Zikry MA, Kao M. Inelastic microstructural failure mechanisms in crystalline materials with high angle grain boundaries. J Mech Phys Solids V 1996;44(11):1765–98.
[12] Arsenlis A, Parks DM. Modeling the evolution of crystallographic dislocation density in crystal plasticity. J Mech Phys Solids 2002;50:1979–2009.
[13] Schafler E, Zehetbauer M, Ungàr T. Measurement of screw and edge dislocation density by means of X-ray Bragg profile analysis. Mater Sci Eng A 2001;319–321:220–3.
[14] Asaro RJ, Rice JR. Strain localisation in ductile single crystals. J Mech Phys Solids 1977;25:309–38.
[15] Gilman JJ, Johnston WG. Observations of dislocation glide and climb in lithium fluoride crystals. J Appl Phys 1956;27:1018–22.
[16] Busso EP. Cyclic deformation of monocrystalline nickel aluminide and high temperature coatings. PhD Thesis, MIT 1990.
[17] Busso EP, McClintock FA. Dislocation mechanics-based crystallographic model of a B2-type intermetallic alloy. Int J Plasticity 1996;12:1–28.
[18] Orowan E. Problems of plastic gliding. Philos Trans Roy Soc London A 1940;52:8–22.
[19] Hibbitt, Karlsson and Sorensen Inc., ABAQUS V6.2, 2001. Providence, RI, USA.
[20] Cheong KS, Busso EP. Modeling the monotonic and cyclic deformation of FCC metals at low homologous temperatures [in preparation].
[21] Kawasaki Y, Takeuchi T. Cell structures in copper single crystals deformed in the [0 0 1] and [1 1 1] axes. Script Metall 1980;14:183–8.
[22] Carreker Jr RP, Hibbard Jr WR. Tensile deformation of high-purity copper as a function of temperature, strain rate, and grain size. Acta Metall 1953;1:654–63.
[23] Kocks UF, Argon AS, Ashby MF. Thermodynamics and kinetics of slip. Progress in materials science, vol. 19. Oxford, UK: Pergamon Press; 1975.
[24] Balasubramaniam S, Anand L. Elasto-viscoplastic constitutive equations for polycrystalline fcc materials at low homologous temperatures. J Mech Phys Solids 2002;50:101–26.
[25] Takeuchi T. Work hardening of copper single crystals with multiple glide orientations. Trans Japan Inst Mater 1975;16:630–9.
[26] Kuhlmann-Wilsdorf D. Theory of plastic deformation : Properties of low energy dislcoation structures. Mater Sci Eng A 1989:113.
[27] Basinski SJ, Basinski ZS. Plastic deformation and work hardening in Dislocations in Solids. In: Nabarro FRN, editor. Dislocation in metallurgy, vol. 4. North-Holland Publishers; 1979. p. 263–362.
[28] Franciosi P, Berveiller M, Zaoui A. Latent hardening in copper and aluminium single crystals. Acta Metall V 1980;28:273–83.
[29] Mader S. Elektronmikroskopische Untersuchung der Gleitlinienbildung auf Kupfereinkristallen. Z Phys 1957;149:73–102.
[30] Rebstock H. Kombinierte Zug-und Torsionsverformung von Kupbfer-Einkristallrohen. Z Metallk 1957;48:206–20.
[31] Müller H, Leibfried G. Die Oberflächenerscheinungen auf gedehnter aluminium-einkristallen in ihrer abhängigkeit von der dehngeschwindigkeit. Z Phys 1955;142:87–115.
[32] Essmann U, Mughrabi H. Annihilation of dislocations during tensile and cyclic deformation and limits of dislocation densities. Philos Mag A 1979;40(6):731–56.
[33] Kawasaki Y. Correspondence between layered cell structures and slip lines in deformed copper single crystals. Jpn J Appl Phys 1979;18:1428–38.
[34] Kelly A, Nicholson RB. Strengthening methods in crystals. London, UK: Elsevier Publishing Co; 1971.
[35] Beaudoin AJ, Acharya A, Chen SR, Korzekwa DA, Stout MG. Consideration of grain-size effect and kinetics in the plastic deformation of metal polycrystals. Acta Mater 2000;48:3409–23.
[36] Delaire F. PhD Thesis, Université Paris-Nord, France 1999.
[37] Hull D, Bacon DJ. Introduction to Dislocations. Oxford, UK: Butterworth-Heinemann; 2001.